Inductively coupled plasma chemistry examinations with visible acousto-optic tunable filter hyperspectral imaging†

Ling Bei,[a] Kirk L. Duffin[b] and Jon. W. Carnahan*[a]

[a]Department of Chemistry and Biochemistry, Northern Illinois University, DeKalb IL 60115, USA. E-mail: carnahan@niu.edu; Fax: 815-753-4802; Tel: 815-753-6879
[b]Department of Computer Science, NIU, DeKalb, IL 60115, USA

Inductively coupled plasma optical emission spectrometry (ICP-OES) is widely used in trace-metal analysis. However, the behavior of this hot, ionized gas and effects on analyte excitation and ionization is not fully understood. To obtain sufficient information on the characteristics of plasma, two previous approaches, Abel inversion and tomography, have been used. Major drawbacks of these approaches include complex optical and data manipulation systems, significant amounts of time required for data collection, and long-term plasma drift and flicker. Initial examinations of an approach to alleviate many of these problems are presented. A hyperspectral imaging (HSI) system using an acousto-optic tunable filter (AOTF) as a wavelength selection device and a charge coupled device (CCD) camera as a detector is described. In these studies, the behavior of a visible paratellurite AOTF is presented. Six elements that yield intense emission lines in the visible wavelength region were examined. With in-house written software, plasma image background correction was achieved in a rapid fashion. Plasma chemistry was studied while varying plasma conditions including the applied rf power, nebulizer sample carrier gas flow, and liquid sample delivery rate. Results indicate that correlations between elemental excitation and ionization energies and the enhancements on emission intensities could be clearly discerned. It is demonstrated that the AOTF-HSI system has the potential to be a powerful tool for plasma chemistry research.

Introduction

Inductively coupled plasma optical emission spectrometry (ICP-OES) is widely used in trace-metals analysis. To better understand and enhance the performance of ICPs, several research groups have examined analyte excitation and energy transfer mechanisms within plasmas.[1–13]

The characteristics of plasmas and discharges can be probed by examinations of their spatial light emission characteristics. Two previous approaches have been used to obtain sufficient information. The first is to obtain multiple discharge radiation intensity measurements. The optics and/or plasma position are adjusted so that incremental vertical and horizontal segments can be sequentially viewed with a monochromator. Using Abel inversion mathematical manipulation techniques, a four-dimensional image (*x, y, z,* and intensity) of the plasma can be constructed. The second approach, tomography, involves isolating a single wavelength with a large-aperture-based monochromator and focusing the radiation upon an array detector. Both techniques are powerful. However, there are drawbacks with each of these approaches, such as the requirement for complex optical and data manipulation systems. The cited Abel inversion approach requires that a large number of time-consuming observations of small spatial volumes be made with sufficient signal-to-noise ratios to produce high quality profiles. The tomographic approach requires that the spectrometer slits be sufficiently wide to conduct image information, resulting in spectral resolution degradation. Both approaches require significant amounts of time and are subject to long-term plasma drift and flicker.

A much more ideal approach would be to obtain multiple, instantaneous, high spectral resolution images of the entire discharge. For the purpose of subtracting out and discerning spectral features from background contributions such as continuum radiation, it should be possible to obtain these images, in rapid fashion, at the wavelength of interest and an adjacent wavelength. A system of this nature should also retain the speed of wavelength access across a broad spectral range. Additionally, the optical aperture should be large to maximize throughput and better accommodate the detection of low light levels. An acousto-optic tunable filter (AOTF) system, constructed with the combination of proper optics and an array detector, has the potential to meet all of these plasma-imaging requirements.

An AOTF is a digitally accessible, compact, variable wavelength optical filter that operates based on the interaction between optical radiation and an acoustic velocity compression or shear wave traversing an anisotropic material. Modern AOTFs are constructed by attaching a piezoelectric transducer to an appropriate crystalline material. The frequency of compression wave application is typically in the tens to hundreds of megahertz range. Interaction between light and the acoustic waves allows photons of a very narrow wavelength range to be diffracted by the AOTF.

The wavelength of light undergoing AOTF diffraction (λ_0) is expressed by equation 1:

$$\lambda_o = \frac{v\Delta n}{f} \sqrt{\sin^4 \theta_i + \sin^2 2\theta_i} \qquad (1)$$

where *v* is the acoustic velocity in the solid medium, Δn is the difference in the refractive indices of the incident and diffracted radiation, *f* is the frequency at which the interaction waves are applied, and Θ_i is the incident angle. Radiation that undergoes AOTF diffraction experiences a 90° polarization rotation and may exit the material at a different angle from that of the incident radiation.

Another important parameter, the bandpass of the diffracted light, is proportional to the wavelength squared; better

This journal is © The Royal Society of Chemistry 2004

J. Anal. At. Spectrom., 2004, **19**, 1–8   1

resolution occurs at shorter wavelengths. More details of AOTF theory may be found in the literature.[14–19]

A number of AOTF device applications for ICP spectrometry have been reported. Fulton and Horlick[20] examined the use of paratellurite AOTFs. Utilizing two AOTF devices, each optimized at the higher and the lower wavelengths of the 350–660 nm spectral region, they characterized the analytical performance for elements such as Ca, Mg, Na, *etc*. The bandpasses ranged from 0.22 nm at 361 nm to 1.6 nm at 660 nm. Gillespie and Carnahan[21] utilized a quartz AOTF to extend the usefulness of the technique to the UV spectral region. The monitored region was 205 to 405 nm. The bandpass of 0.06 nm at 226 nm is moderately acceptable for the requirements of ICP-OES.

In this study, a hyperspectral imaging (HSI) system is constructed with a combination of a visible AOTF, a monochrome CCD camera, and additional appropriate optics. The AOTF-HSI system was previously optimized and characteristic with various light sources, including a continuum source, a tungsten lamp filament, and a line emission source, a Cu hollow cathode lamp with Ne fill gas.[22] The system spatial resolution was examined using a USAF-1951 resolution target.

Six elements (Ca, Cr, Li, Mg, Na and Sr) that yield intense emission lines in the visible wavelength region are used as examples and presented for the plasma chemistry studies. Detailed examinations of effects of the ICP power, nebulizer sample carrier gas flow rate, and liquid sample delivery flow rate were performed. Correlations between elemental excitation and ionization energies and the enhancements of emission intensities were studied.

Experimental

Instrumentation

An ICP-OES-AOTF-HSI system was constructed and is shown in Fig. 1. A Plasmaspec Model 2.5 ICP (Leeman Labs Inc., Hudson, NH) was used with a one-piece quartz torch (Leeman Lab Inc.). An ultrasonic nebulizer (USN, CETAC Technology Inc., Omaha, NE, Model U5000) was used for sample introduction. A peristaltic pump (Rainin Instrument Co. Inc., Woburn, MA) was used to deliver 0.6 mL min^{-1} aqueous samples to the USN and remove waste solvent from the aerosol chamber. The USN Ar carrier gas was generally maintained at a flow rate of 0.92 L min^{-1}, but varied to examine flow rate effects. The plasma Ar coolant flow rate was maintained at

12 L min^{-1}. Radiation from the plasma was directed by a flat mirror and the beam waist was reduced for AOTF introduction with a 5 cm focal length fused silica lens (Oriel Corp., Stratford, CT). The paratellurite AOTF used in this study was purchased from IntraAction Corp. (Model ATF-1102BPJ1). The device has a spectral range of 400–700 nm and a 3 × 3 mm optical aperture. The driver frequency is controlled through a frequency synthesizer (75–150 MHz, 10 kHz resolution, 10 W maximum; Model VFE1004C4, IntraAction Corp.). The combination of a 3 mm diameter round optical aperture preceding the AOTF and radiation collimation helped to avoid the potential internal reflections within the AOTF. After passing through the AOTF, diffracted light was focused with a 10 cm focal length Oriel lens onto the CCD camera (SONY, Model XC-73). A Hauppauge WinTV-Go video capture card (Hauppauge, NY, Model 190) was used for data acquisition.

The AOTF frequency driver and the CCD camera were controlled with a software program written at Northern Illinois University installed in a Dell (Austin, TX) 800 MHz computer. Multispectral scanning was achieved with a graphical user interface through the use of the commercial video digitization hardware. In each interaction of the acquisition process the computer sets the AOTF frequency, grabs four sequential frames and stores them to memory. Images were saved in a single data file, but could be individually extracted.

Reagents

Stock solutions of 100 μg mL^{-1} Ca, Cr, Li, Mg, Na and Sr were prepared using commercially available ICP standards (Inorganic Ventures Inc., Lakewood, NJ) diluted in 1% (v/v) HNO$_3$.

Results and discussion

Optimization of the AOTF-HSI system

A good deal of the optimizations for the described experiments has been reported.[22] Only a summary is reported here. In characterization experiments a continuum source, a tungsten lamp filament, was used to study the effects of AOTF power on hyperspectral image fidelity. A constant frequency of 90.0 MHz (corresponding to 588 nm) was applied. The AOTF driver power was varied from 0.9 to 1.5 W in increments of 0.1 W. The image intensity increased from 0.9 to 1.2 W and leveled off, and the clearest image was obtained at the AOTF power of 1.1 W. Based on comparisons with previous results of applied power on AOTF output,[23] it is likely that the loss of image
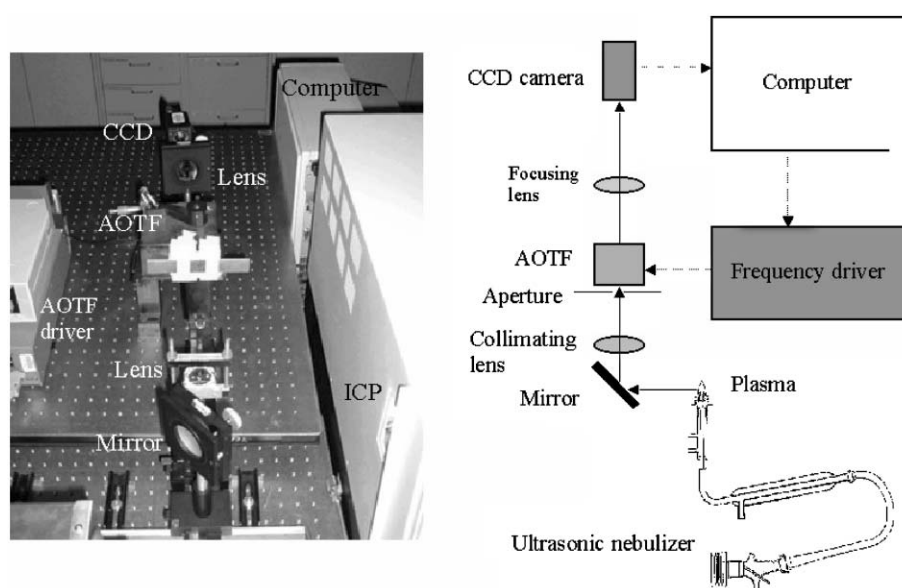

Fig. 1 System diagram of the ICP-AOTF-HSI system.

clarity at higher AOTF driver powers is caused by spurious acoustic wave interactions within the AOTF. Subsequent experiments were conducted at AOTF driver powers in the range of 1.2 W or less.

In order to use the AOTF-HSI for ICP-OES applications, the optical bandpass must be sufficiently narrow. A Cu hollow cathode lamp (HCL) was observed while the AOTF frequency was scanned from 83.0 to 87.0 MHz (corresponding to an 8 nm wavelength range in the 600 nm region) with increments of 0.05 MHz. In this wavelength range, four Ne features were observed, corresponding to Ne line emission at 612.85, 614.31, 616.36 and 618.21 nm. Using in-house developed software, the intensity and wavelength information at every pixel within the HCL image could be obtained. Experimental bandpasses correlated with those previously obtained.[23] It had been shown that the optical bandpass of this particular AOTF is 0.5 nm at 400 nm and 2.5 nm at 700 nm. The applied frequency/wavelength calibration (λ versus $1/f$) was accurate and reproducible, with a second order fit r^2 value of 0.999 94.

AOTFs may exhibit image degradation due to imperfectly collimated light and image shift with changing wavelength.[21,24] Eight pixels were selected across the HCL image for image shifting examination. The image shift was about 1.75 pixel/MHz (or about 0.88 pixel/nm) in this wavelength region. This number is acceptable for most molecular spectrometry studies and for a broader wavelength range, software can be used to calibrate the image shift.

The spatial resolution of AOTF-HSI system was examined with a USAF-1951 resolution target. On this target, groups of test patterns with varying feature sizes appear. The reported resolution is determined by the finest set of features the system can differentiate. Using a tungsten lamp to illuminate the target, an AOTF driver power of 1.2 W and 1 : 1 magnification image optics, the AOTF frequency was incremented from 78 to 108 MHz (corresponding to 670 to 500 nm) as images were captured. Results indicate that the AOTF-HSI has an imaging resolution of 57 cycles mm^{-1} (8.8 μm for each feature) horizontally and 40.3 cycles mm^{-1} (12.4 μm for each feature) vertically. Resolution was unaffected by the AOTF frequency.

Background correction with AOTF-HSI for plasma imaging

Because the plasma exhibits continuum and line background emissions, background corrected analyte emission must be obtained in a rapid fashion. Background corrected images were obtained utilizing a software package called "pnmarith". The "pnmarith" code is open-source software that can be used to perform arithmetic functions on portable anymaps, i.e., image files. The arithmetic functions include addition, subtraction, multiplication, division, etc. Two portable anymaps can be read as inputs, and one portable mathematically manipulated anymap produced. The subtraction function was used for image background correction.

Two background correction approaches were used in this study. The first kind was used to obtain analyte spatial distributions. While the solution containing analyte was nebulized, an online image was obtained at the peak center of the emission line, and an offline image was obtained at a very close wavelength. Fig. 2 shows an example of this background correction approach for Sr atom emission at 460.7331 nm. The online image was chosen at 123.95 MHz (corresponding to 460.73 nm) and the offline image was chosen at 124.50 MHz (corresponding to 458.70 nm). With the two snap shots and the subtraction function, true analyte emission distributions could be obtained.

The second background correction approach was used in studies of plasma parameter alterations. Background correction was done by subtracting the plasma background (while a blank solution was nebulized and the analyte peak center was monitored) from the online analyte signal.

Effects of ICP rf power on analyte spatial behavior

Varying the plasma power will lead to alterations in fundamental plasma parameters such as temperatures and electron distributions. To study the effects of ICP rf power on the analytical behavior, a power range was selected from the lowest power which would maintain the plasma up to the highest power which would not damage the plasma torch. Within the six elements used in this research, the emission from some elements, such as Na and Mg, saturated the CCD detector at 255 counts when the ICP power reached to 1.40 kW, making the data unusable. In these cases, these elements were studied in the ICP power range up to 1.21 kW. For other elements, such as Ca, Cr, and Li, the ICP power data up to 1.40 kW is presented. For Sr, a power of up to 1.60 kW could be utilized.

Sample solutions (100 μg mL^{-1}) of Ca, Cr, Mg, Li, Sr and Na were nebulized while using a constant USN carrier gas flow rate of 0.92 L min^{-1}. The Ar coolant flow rate was maintained at 12 L min^{-1}, the liquid sample delivery rate was set at 0.60 mL min^{-1}. Fig. 3 shows the background corrected images of these elements while the ICP rf power was increased. The results for their emission intensities in both the preheating and normal analytical zones at the lowest and highest powers are listed in Table 1. For reference, the preheating zone is defined as the integrated region from 0 to 5 mm below the load coil; the normal analytical zone is defined from 0 to 20 mm above the load coil. Averaged intensities are reported.

Within the elements listed in Table 1, various behaviors were observed. For lower ionization energy elements, such as Na, Li, and Sr, the overall emission intensities in both the preheating (ranging from factors of 0.02 to 0.48) and normal analytical
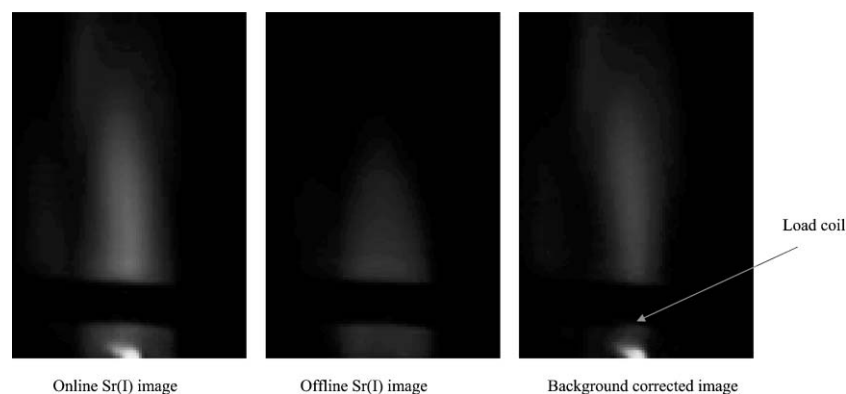

Fig. 2 Online, offline and background corrected images of Sr atom line emission 460.73 nm. The AOTF frequency for Sr atom line emission is 123.95 MHz (460.73 nm) for online and 124.50 MHz (458.70 nm) for offline images.
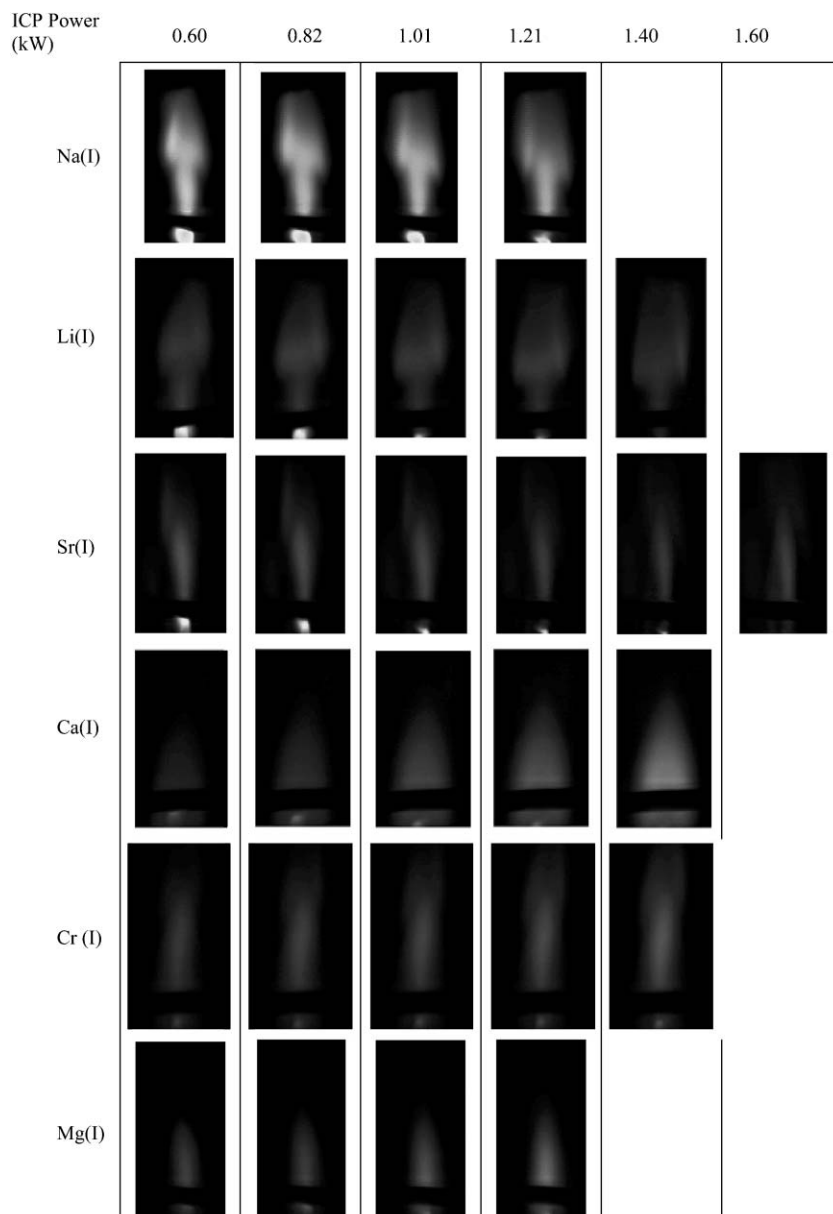
Fig. 3 Effects of ICP rf power on selected elements.

zones (ranging from factors of 0.20 to 0.75) decreased as the ICP power was increased. However, for higher ionization energy elements, such as Ca, Cr, and Mg, the overall emission intensities increased as the ICP power was increased, and greater enhancements were observed in the normal analytical zone (ranging from factors of 2–5) than in the preheating zone (ranging from factors of 1–2). These behaviors can be

explained by examinations of ionization and excitation of each element.

For lower ionization energy elements, such as Na, Li and Sr, at lower ICP powers, the plasma provides sufficient energy to excite the atoms. At higher ICP powers, depending upon the element, the kinetically limited ionization processes may proceed to a greater degree, increase the ion populations,

Table 1 Effects of ICP rf power on emission intensities in the preheating and the normal analytical zones

	Preheating zone			Normal analytical zone				
	Emission intensity (counts)			Emission intensity (counts)				
Element and wavelength/nm	Low power[a]	High power[a]	Ratio	Low power[a]	High power[a]	Ratio	E_{ion}/eV	E_{ex}/eV
Na I—589.598	250	120	0.48	240	180	0.75	5.14	2.11
Li I—610.362	250	5	0.02	50	10	0.20	5.39	4.45
Sr I—460.733	230	20	0.09	60	20	0.33	5.69	2.67
Ca I—422.673	50	50	1.00	10	50	5.00	6.11	4.73
Cr I—520.604	30	50	1.67	30	60	2.00	6.77	3.36
Mg I—518.362	50	50	1.00	20	50	2.50	7.56	5.14

[a] The ICP rf power was varied at different range for different elements. For all the elements, the lowest power is 0.60 kW, for Ca, Cr, and Li, the highest power is 1.40 kW; for Mg and Na, the highest power is 1.21 kW; for Sr, the highest power is 1.60 kW.
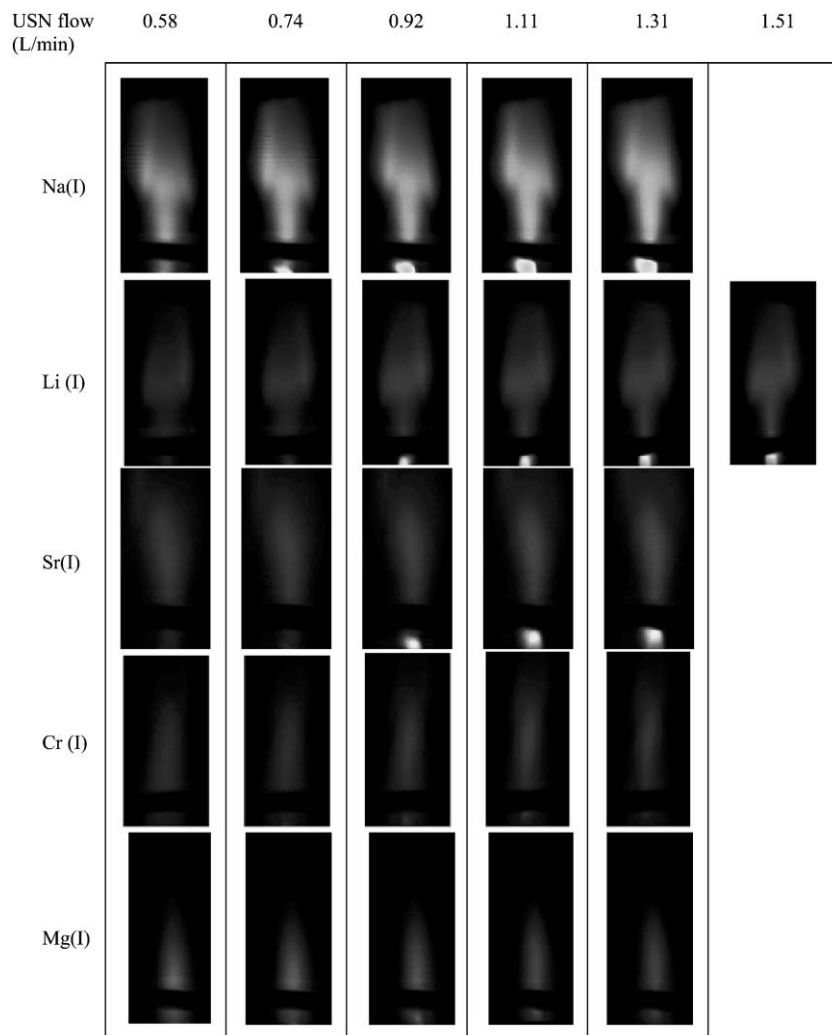
Fig. 4 Effects of USN sample carrier gas flow rate on selected elements.

and decrease the atom populations. The decreases in atom emission intensity are less significant in the normal analytical zone (farther from the hottest portion of the plasma and away form the preheating zone near the load coil). This result indicates that power more significantly affects these lower ionization energy elements near the load coil.

For higher ionization energy elements (Mg, Cr and Ca), the atom emission intensities increased as the ICP power was increased. The effects of enhancement in atom signal with increased power was greater in the normal analytical zone. This result indicates that ionization effects are less significant for these elements and that the improvement in excitation environment at higher powers dominates the chemistries of these elements. In the preheating zone, the most intense spot moved away from the load coil as the power was increased. This observation indicates that the excitation capabilities of the preheating zone expanded as the ICP power was increased.

Effects of USN sample carrier gas flow rate on analyte spatial behavior

The USN analyte mist carrier Ar flow rate will influence the analyte residence time in the plasma and the amount of sample aerosol that reaches the plasma. The Ar coolant flow rate was maintained at 12 L min^{-1} and the ICP power was set at 1.01 kW. The liquid sample delivery rate was maintained at 0.6 mL min^{-1}. Analyte solutions of 100 µg mL^{-1} Cr, Li, Mg, Sr, and Na were nebulized. Because of the CCD saturation problem, the maximum usable USN sample carrier gas flow rate varied for different elements. The lowest rate was 0.58 L min^{-1}.

For Cr, Mg, Na, and Sr, the highest flow rate was 1.31 L min^{-1}; for Li, the highest flow rate was 1.51 L min^{-1}. For the quartz plasma torch with a nominal 1.0 mm inner diameter sample injection orifice, the orifice velocity of the analyte can be calculated. Translating this velocity to analyte residence time in a 1.00 cm vertical observation zone of the plasma, analyte time in this observation zone is 0.81 ms at a flow rate of 0.58 L min^{-1} and 0.31 ms at a gas flow rate of 1.51 L min^{-1}.

Fig. 4 illustrates analyte spatial behavior as the USN sample carrier flow rate was increased. The results for emission intensities in both the preheating and the normal analytical zones at the lowest and highest sample carrier gas flow rate are listed in Table 2. Besides Mg, the emission intensities of all elements increased as the USN sample carrier gas flow rate was increased. The different behaviors of these elements can be explained by examinations of their ionization and excitation energies.

As described, the USN sample carrier gas flow rate will influence the residence time and the amount of sample aerosol which reaches the plasma. For lower ionization energy elements, atom emission intensities increase with increasing flow rates in both the preheating and normal analytical zones. This is caused by the increasing amount of analyte being carried into the plasma at greater gas flow rates. However, for Mg, the atoms do not have sufficient energy to be excited. With an increased flow rate, the residence time decreases. This leads to a decrease in intensity both in the preheating and normal analytical zones.

Evidence exists pointing to a combination of increased analyte delivery to the plasma with a concomitant decrease in

Table 2 Effects of USN sample carrier gas flow rate on emission intensities in the preheating and normal analytical zones

Element and wavelength/nm	Preheating zone			Normal analytical zone			E_{ion}/eV	E_{ex}/eV
	Emission intensity (counts)			Emission intensity (counts)				
	Low rate[a]	High rate[a]	Ratio	Low rate[a]	High rate[a]	Ratio		
Na I—589.598	60	250	4.17	80	240	3.00	5.14	2.11
Li I—610.362	10	200	20.0	10	50	5.00	5.39	4.45
Sr I—460.733	20	240	12.0	40	60	1.50	5.69	2.67
Cr I—520.604	20	50	2.50	10	40	4.00	6.77	3.36
Mg I—518.362	50	30	0.60	60	40	0.67	7.56	5.14

[a] The USN gas flow rate was varied at different range for different elements. The lowest flow rate is 0.58 L min^{-1}, for Cr, Mg, Na, and Sr, the highest flow rate is 1.31 L min^{-1}; for Li, the highest flow rate is 1.51 L min^{-1}.

analyte ionization as the gas flow rate is increased. In the preheating zone, atom emission enhancements for elements of lower ionization energies (Na(I), Li(I), and Sr(I)) are great. Higher in the discharge, enhancements for these elements are less. That the plasma region exhibiting the greatest ionization effects, the preheating zone, is much more affected by the increase in flow rates, indicates that ionization chemistry is the dominant factor. For Mg, which is difficult to excite, it appears that the dominant effect may be that of decreased plasma excitation capability at higher flow rates.

Also, for all the elements studied in this test, the most intense spot in the preheating zone "moved" closer to the load coil as the USN carrier gas flow rate was increased. This is caused by the increase of analyte mist velocities as the carrier gas flow rate was increased. As the analyte atoms were pushed through the plasma more quickly at greater flow rates, excitation occurred in the region closer to the load coil.

Effects of liquid sample delivery rate on analyte spatial behavior

With a constant USN gas flow rate, an increase of the liquid sample delivery rate will increase the amount of sample aerosol directed to the plasma. The ICP power was set at 1.01 kW, the Ar coolant flow rate was maintained at 12 L min^{-1}, and the Ar carrier gas flow rate was set at 0.92 L min^{-1}. The sample solutions (100 µg mL^{-1}) of Ca, Cr, Li, Na, Mg and Sr were directed to the USN with a peristaltic pump, and the liquid delivery rate was varied from 0.30 to 1.50 mL min^{-1}. Fig. 5 illustrates the effects of sample delivery rate on spatial emission behavior of the selected elements.

Table 3 shows the enhancements in emission intensities in both the preheating and normal analytical zones at the lowest and highest liquid sample delivery rate. Overall, an increase in emission intensity was observed in both zones for all these elements as the liquid sample delivery rate was increased from 0.3 to 1.5 mL min^{-1}. In the normal analytical zone, the emission intensities increase ranged from a factor of 1.67 to 16. In the preheating zone, the emission intensities increase ranged from a factor of 1.31 to 18. These results indicate that as the liquid sample delivery rate is increased, the total amount of analyte introduced into the plasma increased.

There appears to be a strong correlation of enhancement ratios with the excitation energies of the elements. For example, in the preheating zone, the three atomic species with the greatest excitation energies (Mg I, Ca I, and Li I) exhibit large enhancements (from 4 to 18 fold) as the liquid delivery rate is increased, and the enhancement ratio decreased in the normal analytical zone. For other elements with lower excitation energies (Na I, Sr I, and Cr I), the enhancements are less in the preheating zone, but increase in the normal analytical zone.

The behaviors can be explained with reference to the temperature differences in the preheating and normal analytical zones. The preheating zone is closer to the plasma core, and has a higher temperature than the normal analytical zone. Besides intensity increases, the size of the most intense region in

the preheating zone grows as the liquid sample delivery rate is increased. This is caused by the increasing amounts of analyte being delivered into the plasma. For higher excitation energy elements, as the analyte is carried upstream in the plasma the local temperature drops, which leads to a decrease of excitation. Because of this, for higher excitation energy elements, although the overall emission intensity in the normal analytical zone increases as the sample delivery rate is increased, the enhancements for these elements in the normal analytical zone are less than the enhancements in the preheating zone. On the other hand, for lower excitation energy elements, the temperature in the normal analytical zone
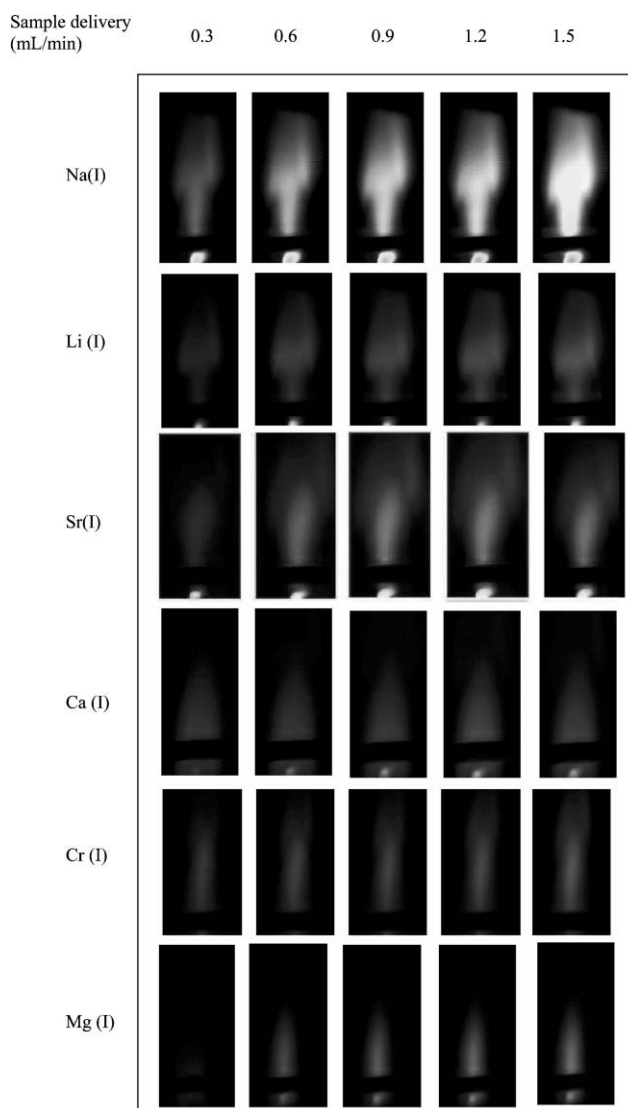

Fig. 5 Effects of liquid sample delivery rate on selected elements.

Table 3 Effects of sample delivery rate on emission intensities in the preheating and normal analytical zones

| Element and wavelength/nm | Preheating zone Emission intensity (counts) | | | Normal analytical zone Emission intensity (counts) | | | E_{ion}/eV | E_{ex}/eV |
	0.3 mL min^{-1}	1.5 mL min^{-1}	Ratio	0.3 mL min^{-1}	1.5 mL min^{-1}	Ratio		
Na I—589.598	190	250	1.32	70	250	3.57	5.14	2.11
Li I—610.362	10	70	7.00	90	150	1.67	5.39	4.45
Sr I—460.733	160	240	1.50	30	90	3.00	5.69	2.67
Ca I—422.673	20	100	5.00	20	40	2.00	6.11	4.73
Cr I—520.604	30	60	2.00	30	70	2.33	6.77	3.36
Mg I—518.362	5	90	18.0	5	80	16.0	7.56	5.14

provides sufficient energy to excite the atoms. Large enhancements were observed in the normal analytical zone as well as the preheating zone.

While the trends with the present elements are clear, further examinations are required to develop correlations and relationships to the plasma chemistry.

Conclusions

Results presented in this article illustrate the possibilities and advantages of AOTF-HSI applications for ICP imaging. Combined with a visible AOTF, a CCD camera and in-house developed software, the AOTF-HSI system can change wavelengths quickly and provide high quality hyperspectral images. While the spectral resolution of the described visible system is only moderate, it is quite adequate for spectral regions relatively uncluttered by intense molecular and line background emission. With background correction software, analyte emission distributions in the plasma can be acquired in a rapid fashion.

The effects of variations of a number of parameters on the chemistry of selected elements were examined. The observations indicate that the ionization and excitation energies play an important role in the spatial behavior of these elements.

AOTF hyperspectral imaging is a powerful tool which can be used in ICP-OES, especially plasma imaging. With quick wavelength access capabilities and large optical apertures, elements which yield intense plasma emission in the visible spectral wavelength region were successfully imaged. The chemistry of the entire plasma can be quickly studied and behavioral characteristics elucidated with this approach. This technique can easily be utilized to study other discharges. With respect to ICP-OES, most elements have more intense line emissions in the UV wavelength region and work is currently being performed in our laboratories to examine the UV spectral region using a quartz AOTF. It is expected that AOTF systems of this nature can provide information complementary to currently existing plasma diagnostic approaches.

Acknowledgements

References

1 J. A. Horner and G. M. Hieftje, *Appl. Spectrosc.*, 1999, **53**(6), 713–718.
2 D. A. Solyom, T. W. Burgoyne and G. M. Hieftje, *J. Anal. At. Spectrom.*, 1999, **14**(8), 1101–1110.
3 C. A. Monning, K. A. Marshall, G. D. Rayson and G. M. Hieftje, *Spectrochim. Acta, Part B*, 1988, **43**(9–11), 1217–1233.
4 E. H. Choot and G. Horlick, *Spectrochim. Acta, Part B*, 1986, **41**(9), 935–945.
5 C. D. Skinner and E. D. Salin, *J. Anal. At. Spectrom.*, 1997, **12**(10), 1131–1138.
6 J. Babis, M. J. Pilon and M. B. Denton, *Appl. Spectrosc.*, 1990, **44**(7), 1281–1289.
7 A. S. Al-Ammar and R. M. Barnes, *At. Spectrosc.*, 1998, **19**(1), 18–23.
8 A. Montaser, I. Ishii, B. A. Palmer and L. R. Layman, *Spectrochim. Acta, Part B*, 1990, **45**(6), 603–612.
9 A. Lazar and P. Farnsworth, *Appl. Spectrosc.*, 1997, **51**(5), 617–624.
10 P. B. Farnsworth, B. W. Smith and N. Omenetto, *Spectrochim. Acta, Part B*, 1991, **46**(6), 843–850.
11 K. Eland, D. Stratis, D. Gold, S. Goode and S. M. Angel, *Appl. Spectrosc.*, 2001, **55**(3), 286–291.
12 J. W. Olesik, J. A. Kinzer and M. P. Dziewatkoski, *Spec. Publ. Roy. Soc. Chem.*, 1997, **202**, 1–12.
13 J. W. Olesik, C. Hensman, S. Rabb and D. Rago, *Spec. Publ. Roy. Soc. Chem.*, 2001, **267**, 3–16.
14 C. D. Tran, *Anal. Chem.*, 1992, **64**, 971A–981A.
15 J. Lekavich, *Basics of Acousto-Optic Device, Lasers and Applications*, 1996, pp. 59–64.
16 J. Xu and R. Stroud, *Acousto-Optic Devices. Principles, Design, and Applications*, John Wiley and Sons, New York, 1992, ch. 7.
17 A. Korpel, *Acousto-Optics*, Marcel Dekker: New York, 1988.
18 A. P. Goutzoulis and D. R. Rape, *Design and Fabrication of Acousto-Optic Devices*, Marcel Dekker: New York, 1994, ch. 4.
19 L. Bei, G. I. Dennis, H. M. Miller, T. W. Spaine and J. W. Carnahan, *J. Quant. Elect.*, 2004, **28**(2), 67–87.
20 G. Fulton and G. Horlick, *Appl. Spectrosc.*, 1996, **50**(7), 885–892.
21 S. R. Gillespie and J. W. Carnahan, *Appl. Spectrosc.*, 2001, **55**(6), 730–738.
22 L. Bei, *PhD Dissertation*, Northern Illinois University, 2004.
23 E. G. Bucher and J. W. Carnahan, *Appl. Spectrosc.*, 1999, **53**(5), 603–611.
24 D. A. Glenar, J. J. Hillman, M. Lelouarn, R. Q. Fugate and J. D. Drummond, *Publ. Astron. Soc. Pacific*, 1997, **109**, 326–332.

JAAS Proofs for correction

Authors Queries

Paper: **b404128c**

Please check the proofs of your paper carefully. **Your proofs will not be read in detail by staff after you have returned them to us.** It is your responsibility to ensure that the proofs have been read carefully.

Translation errors between word-processor files and typesetting systems can occur so the whole proof needs to be read even if an electronic file has been supplied. Please pay particular attention to: tabulated material (this may have been rekeyed); equations; numerical data; figures and graphics; and references. If you have not already done so and wish to indicate the corresponding author(s) please mark their name(s) with an asterisk. Please fax or e-mail your corrections to us where possible.

This proof reflects the content and general style of the paper without the stylistic complexity of the final printed page; however, the only differences should be minor layout changes such as different line breaks, tables being double column instead of single column and improvements in graphic placement.

We will endeavour to publish the article electronically on the RSC web site as soon as possible after we receive your corrections. **NB: No late corrections can be made hence please ensure that only your final corrections are notified to us.**

Please return you **final** corrections, where possible within **48 hours** of receipt to:

Mrs Sarah James, Serials Production, The Royal Society of Chemistry,
Thomas Graham House, Science Park, Milton Road, Cambridge, UK, CB4 0WF.
Tel: +44 (0)1223 432362; Fax: +44 (0)1223 432160; E-mail: proofs@rsc.org

Reprints—Electronic (PDF) reprints will be sent free of charge to the corresponding author. Enquiries about purchasing paper reprints should be addressed to: Miss Susan Bull, Production Operations Department, (at the RSC Cambridge address given above).